Boundary-Layer Meteorology (2024) 190:33
https://doi.org/10.1007/s10546-024-00872-y

RESEARCH ARTICLE

Locally Stationary Wavelet Analysis of Nonstationary Turbulent Fluxes

D. Arias-Arana[1,4] · G. J. Fochesatto[2] · R. Jimenez[3] · C. Ojeda[1]

Received: 17 February 2024 / Accepted: 14 June 2024 / Published online: 15 July 2024

Abstract
We propose the multivariate locally stationary wavelet (mvLSW) process to analyze surface turbulent fluxes in nonstationary atmospheric conditions. Using theoretical spectral characteristics, we generated synthetic data representing stationary and nonstationary turbulence time series. This data enables us to explore the impact of mesoscale atmospheric flows on the stationary microscale turbulence field and detect the spectral gap in the time-varying cospectra. Applying this approach to experimental data collected in Fairbanks, Alaska and Bogota, Colombia, we demonstrated the ability to detect cospectral gaps and compute bandwidth-limited turbulent fluxes arising from stationary components of the atmospheric flow. These findings underscore the importance of considering scale-dependent atmospheric forcing when comparing model and experimental data.

Keywords Land-surface atmosphere interactions · Surface turbulent fluxes · Multivariate locally stationary wavelet process · Nonstationary time series · Spectral gap

1 Introduction

The cross-covariance of turbulent time series allows computing the turbulent fluxes in the atmospheric surface layer (ASL) (Stull 1988). Such estimates and their interpretation depend upon the assumption that cross-covariances time series are stationary (Arya and Holton 2001). However, this assumption can be compromised when multiple atmospheric scales affect the atmospheric flow during the computation period. In order to detect the impacts of low-frequency atmospheric scales, the ogive test function is often applied to determine

✉ D. Arias-Arana
diego.andres.arias@correounivalle.edu.co

C. Ojeda
cesar.ojeda@correounivalle.edu.co

1 Faculty of Engineering, School of Statistics, Universidad del Valle-Cali, Cali 760032, Colombia

2 Department of Atmospheric Sciences, College of Natural Science and Mathematics, University of Alaska Fairbanks, 1930 Yukon Drive, Fairbanks, AK 99775, USA

3 Department of Chemical and Environmental Engineering, Universidad Nacional de Colombia-Bogota, Bogota DC 111321, Colombia

4 Centre for Bioinformatics and Photonics (CIBioFi), Universidad del Valle, Cali 760032, Valle del Cauca, Colombia

nonstationarity in turbulent cross-covariance time series (Foken and Kramm 1995; Oncley et al. 1996). Under stationary atmospheric flow, such test converges to the cross-covariance value as frequency decreases (Foken and Kramm 1995). Identifying the frequency where this convergence begins defines an optimal averaging timescale to compute the turbulent fluxes (Oncley et al. 1996). However, if such convergence does not occur, a finite cross-covariance cannot be defined, indicating nonstationarity in the turbulent time series (Shumway and Stoffer 2017). For instance, nonstationary atmospheric flows can also be present during morning transitions when turbulent sensible heat flux turns positive over time (Oncley et al. 1996; Angevine et al. 2020). Similarly, nonstationarity can also manifest when observational time series reveals local influence of the atmospheric flows with limited sampling of mesoscale motions in stable atmospheric conditions (Vickers and Mahrt 2003; Acevedo et al. 2014). Thus, it seems necessary to better understand the impact and interplay of the atmospheric forcing scales affecting surface turbulent fluxes when such nonstationary behavior is verified.

The wavelet transform has been extensively used to analyze nonstationarity in turbulence time series (Farge 1992; Collineau and Brunet 1993a). Wavelet functions, explored by Collineau and Brunet (1993a), reveal patterns in univariate time series. They were also able to identify ramp-like patterns in fast temperature observations associated to the occurrence of coherent structures (Collineau and Brunet 1993b; Starkenburg et al. 2013) and segregate low-frequency components in wind speed and temperature signals via data reconstruction and filtering (Katul and Vidakovic 1996). Alternatively, Howell and Mahrt (1997) adopted a bivariate multiresolution decomposition wavelet (Mallat 1989) to identify the contributions to atmospheric fluxes from different timescales. Through this technique, Vickers and Mahrt (2003) identify the cospectral gap and quantify the mesoscale and local turbulence contributions to the heat flux. Similarly, Acevedo et al. (2014) determines timescale of submesoscale processes on turbulence, identifying power-law relationships in the multiresolution spectra and cospectra. After that, Babić et al. (2017) uses Voronovich and Kiely (2007) to determine the spectral gap in datasets acquired in complex terrain. They found a convergence in the spectral gap value when evaluating datasets from anemometers as a function of height. Based on this convergence they proposed a running mean where the time-window depends on the spectral gap obtained thus, separating the low varying terms from the turbulence field. And, more recently, Lehner and Rotach (2023) analyzed turbulence datasets using the method developed by Vickers and Mahrt (2003) and Voronovich and Kiely (2007) to detect the spectral gap. Then, using similarity relationships, they found a function where the spectral gap is expressed as a function of wind speed and stability parameter z/L. From this function a time-dependent cutoff frequency filter was found to detrend the signals and thus separate non-turbulent components from the signal. In conclusion, multiresolution wavelet analysis has been demonstrated to be able to disentangle time-variations and energy contributions of oscillation modes and localized structures across time and space (Farge 1992; Torrence and Compo 1998).

We investigate the applicability of the multivariate locally stationary wavelet (mvLSW) process in the framework of nonstationary turbulence time series analysis. Section 2 introduces the theoretical framework of the mvLSW process, providing its interpretation in a turbulence context. Section 3 outlines simulation scenarios for both stationary and nonstationary conditions to aid in interpreting experimental results. Then, we are able to generate stationary—similarly to Hojstrup (1993)—and nonstationary time series, where the nonstationarity can be introduced on any atmospheric scale (micro and mesoscale). In this work, we created the nonstationary scenario by combining spectral and cospectral contributions of a mesoscale atmospheric signal with theoretical contributions to the stationary microscale. We use this synthetic signal to illustrate spectral gap detection and separation of atmospheric

processes at different scales. In Sect. 4, we apply the mvLSW process over real atmospheric datasets to obtain turbulent sensible heat flux in tropical regions (e.g., Bogota, Colombia) and in high-latitude continental areas during winter (e.g., Fairbanks, Alaska). Similarly, in "Appendix 1", the momentum fluxes—turbulent velocity field covariances and cross-covariances—are illustrated for Fairbanks. Finally, Sect. 5 discusses potential applications of the methodology and provides concluding remarks.

2 Multivariate Locally Stationary Wavelet Processes for Turbulent Time Series

This section introduces the mvLSW processes described in Park et al. (2014). The model represents the turbulence time series as a linear combination of wavelet functions multiplied by the transfer matrix. Through this matrix, we obtain the time-varying spectrum and cospectrum across time scales, allowing the reconstruction of a bandwidth-limited variance and cross-covariance signal. By defining the scales containing the microscale, we can reconstruct the cross-covariance signal associated with the turbulent flux. Additionally, the mvLSW processes allow simulating turbulence time series with theoretical spectral characteristics useful for generating synthetic turbulence signals based on hypothetic atmospheric conditions.

The assembly of turbulent time series forms a matrix with P columns, $\mathbf{X}_{t;T} = \left[X^{(1)}_{t;T}, X^{(2)}_{t;T}, \ldots, X^{(P)}_{t;T}\right]'$. Each column represents a turbulent time series of dyadic length $T = 2^J$ for some $J \in \mathbb{N}$ and the scale $j \in \{1, 2, \ldots, J\}$. For example, when analyzing the kinematic heat flux $\overline{w'\theta'}$, there are two time series ($P = 2$). One time series is vertical wind speed fluctuations $X^{(1)}_{t;T} = w'$, and the other is the sonic temperature fluctuations $X^{(2)}_{t;T} = T'_s$. The mvLSW process for the turbulence time series $\mathbf{X}_{t;T}$ is outlined as follows:

$$\mathbf{X}_{t;T} = \sum_{j=1}^{J} \sum_{k} \mathbf{V}_j(k/T)\psi_{j,t-k}\mathbf{z}_{j,k}, \tag{1}$$

where $\{\psi_{j,t-k}\}_{jk}$ is a set of discrete non-decimated wavelets covering the entire time domain, i.e., $k \in \mathbb{Z}$ (Chui 1992; Nason 2008). $\mathbf{V}_j(k/T)$ is the transfer function matrix and $\mathbf{z}_{j,k} = [z^{(1)}_{j,k}, \ldots, z^{(P)}_{j,k}]$ represents random orthonormal increment sequences with mean vector $\mathbf{0}$ and $\mathrm{cov}\left(z^{i}_{j,k}, z^{i'}_{j',k'}\right) = \delta_{i,i'}\delta_{j,j'}\delta_{k,k'}$ (Park et al. 2014). To explain Eq. (1), we consider the locally stationary process for one dimension, when $P = 1$. The time series $X_{t;T}$, for clarity, can be expressed as $X_{t;T} = \sum_{j=1}^{J}\sum_{k} \tilde{w}^0_{j,k;T}\psi_{j,t-k}$—a linear combination of wavelet functions multiplied by random amplitudes (Nason et al. 2000)—where $\tilde{w}^0_{j,k;T} = w^0_{j,k;T}z_{j,k}$, and $\{w^0_{j,k;T}\}$ are the set of amplitudes, and $\{z_{j,k}\}$ is a set of uncorrelated random variables (Nason et al. 2000). By replacing the set $\{\psi_{j,t-k}\}_{jk}$ with the harmonic functions $\{\exp(in\omega t)|\omega \in [-\pi, \pi], n \in \mathbb{Z}\}$, we can obtain a form of the time series in Fourier representation as $X_t = \sum_{n=-\infty}^{\infty} c_n \exp(in\omega t)$ where c_n are the amplitudes (Chui 1992). However, harmonic functions can only represent the frequency domain and may limit their ability to capture time-specific features in atmospheric turbulence records (Strunin and Hiyama 2004). Thus, wavelets are the right mathematical approach, especially when considering nonstationary time series cases, given their compact support. A quick introduction to wavelets can be found in Chui (1992), and their application in atmospheric records, in Torrence and Compo (1998).

Within this framework, the matrix $\mathbf{V}_j(k/T)$ contains the contribution to time-varying variances (on-diagonal terms) from each turbulence time series and, also, captures the interdependence between these time series in the time-varying cross-covariance (off-diagonal terms). Each element of $\mathbf{V}_j(k/T)$ is assumed to be a Lipschitz continuous function. This condition makes possible to define fluxes locally and quantify its variations over time (Nason et al. 2000; Park et al. 2014). Based on $\mathbf{V}_j(k/T)$, Park et al. (2014) define the local wavelet spectral (LWS) matrix at scale j and rescaled time $u = kT^{-1}$ as shown in Eq. (2): The transpose of $\mathbf{V}_j(k/T)$ is denoted as $\mathbf{V}_j^\top(k/T)$:

$$\mathbf{S}_j(u) = \mathbf{V}_j(u)\mathbf{V}_j^\top(u). \tag{2}$$

In a neighborhood around time interval $u \in (0, 1)$ at scale j, $\mathbf{S}_j(u)$ measures the local average power of each turbulent time series and their interdependence—the contribution to variance and cross-covariance. Following Eq. (2), the diagonal elements $S_j^{(p,p)}(u)$ are the spectrum of individual turbulence time series, while the off-diagonal elements $S_j^{(p,q)}(u)$ depict the cospectrum between time series. Here, $p, q \in \mathcal{N}_1^P$ act as indices for turbulent time series within the matrix $\mathbf{X}_{t;T}$.

Following Park et al. (2014), we estimate $\mathbf{S}_j(u)$ via the wavelet periodogram matrix $\mathbf{I}_{j,k} = \mathbf{d}_{j,k}\mathbf{d}_{j,k}^\top$, where the coefficient vector $\mathbf{d}_{j,k} = \sum_{t=0}^{T-1} \mathbf{X}_t \psi_{j,k}(t)$ are the empirical wavelet coefficient. The expected value of the estimator of $\mathbf{S}_j(u)$—i.e., $\mathbf{I}_{j,k}$—differs of the target quantity $\mathbf{S}_j(u)$ and, therefore, $\mathbf{I}_{j,k}$ is a biased estimator. Additionally, $\mathbf{I}_{j,k}$, as T tends to be infinite, fails to converge—in terms of probability—to $\mathbf{S}_j(u)$, implying that $\mathbf{I}_{j,k}$ is an inconsistent estimator. As a result, bias and inconsistency are undesirable statistical properties because of the inherent statistical inference process. Similarly, to the problem of estimating the spectral density function with harmonics functions (Priestley 1982), the estimator $\mathbf{I}_{j,k}$ can be smoothed and corrected to obtain an estimator asymptotically unbiased and consistent—details in Park et al. (2014). For clarity, we denote the asymptotically unbiased and consistent estimator of $\mathbf{S}_j(u)$ as $\hat{\mathbf{S}}_j(u)$. Now, considering $\hat{\mathbf{S}}_j(u)$ and that the signal has a finite length size T, difficulties arise when estimating the spectral contribution of the signal around its boundaries since these estimates are highly uncertain due to the amount of data available for such an estimation. Therefore, considering these limitations, we compute a curve-dashed line that indicates the spectral and cospectral region reliable (estimated with a 95% level of confidence)—the cone of influence described by Torrence and Compo (1998).

Therefore, based on the elements $S_j^{(p,q)}(u)$, we obtain the local cross-covariance band-limited—from scale m_0 to m—between time series p and q at lag τ as follows,

$$c_{m_0,m}^{(p,q)}(u, \tau) = \sum_{j=m_0}^{m} S_j^{(p,q)}(u)\Psi_j(\tau). \tag{3}$$

Notably, we obtain the local autocovariance when $p = q$. The collection of discrete non-decimated wavelets functions are represented by the discrete autocorrelation wavelet $\Psi_j(\tau) = \sum_k \psi_{j,k}\psi_{j,k-\tau}$ (Eckley and Nason 2005). An interesting feature of $\Psi_j(\tau)$ is evident at $\tau = 0$, where $\Psi_j(0) = 1$ implies $c_{m_0,m}^{(p,q)}(u, 0) = \sum_{j=m_0}^{m} S_j^{(p,q)}(u)$ (Nason et al. 2000; Sanderson et al. 2010). In this representation, Eq. (3) reconstructs the local cross-covariance between scales m_0 to m with $m > m_0$. Specifically, the total local cross-covariance appears when $m_0 = 1$ and $m = J$. Then, the integrated cross-covariance limited to scales m_0 and m

is,

$$\langle c_{m_0,m}^{(p,q)} \rangle = \int_0^1 c_{m_0,m}^{(p,q)}(u,0)du = \int_0^1 \left(\sum_{j=m_0}^{m} S_j^{(p,q)}(u) \right) du. \tag{4}$$

The mvLSW process, as indicated in Eq. (1), can represent cross-covariances among turbulent time series, e.g., (w', T_s'). Subsequently, such P-variate time series can be described by a LWS matrix to depict their spectral and cospectral properties with Eq. (2) across time and scale. The importance of this duality time-scale emerges in Eq. (3), where the original cross-covariances can be reconstructed over time, accounting for a sub-band or a full cospectral process representation. This aspect allows us to obtain turbulent fluxes considering only the microscale atmospheric motion, assuming we have a known scale gap. This approach might disentangle stationary from nonstationary processes embedded in the cross-covariance signal, while Eq. (4) estimates the cumulative turbulence flux (e.g., $\overline{w'T_s'}$).

3 Statistical Simulation of Nonstationary Turbulent Signals

To demonstrate estimating atmospheric turbulence fluxes in nonstationary conditions, we simulate a bivariate turbulent time series using the mvLSW process. These simulated signals exhibit spectral and cospectral features outlined by an idealized LWS matrix $\mathbf{S}_j(u)$ (Park et al. 2014; Taylor et al. 2019). The theoretical $\mathbf{S}_j(u)$ includes both stationary and nonstationary contributions according to the proposed conceptual model. We assume that the stationary contribution originates from stationary and isotropic turbulence (Vercauteren et al. 2019). However, the nonstationary contribution arises from the presence of mesoscale motions (Vickers and Mahrt 2003; Acevedo et al. 2014) where a known scale gap separates these contributions (Stull 1988; Vickers and Mahrt 2003).

3.1 A Conceptual Model for Spectral and Cospectral Turbulence Characteristics

In the ASL, turbulent fluxes are influenced by microscale and mesoscale processes. Therefore, the fluxes can be conceptually idealized as composed of functions representing embedded time-scale processes and their associate spectral and cospectral variations according to,

$$\mathbf{S}_j(u) = \mathbf{S}_{\text{micro},j}(u) + \mathbf{S}_{\text{meso},j}(u) + \mathbf{S}_{\text{meso}\leftrightarrow\text{micro},j}(u), \quad \text{for} \quad u \in (0,1). \tag{5}$$

In fact, Eq. (5) is a generalization of Reynolds decomposition where the mean (a low-frequency signal) is separated from the turbulent component (a high-frequency signal). However, such decomposition can only be expressed in the well-known two terms—mean and turbulence—, assuming that the spectral gap exists. Nevertheless, when across scale interactions are present in the time series, we have to enable the third term, $\mathbf{S}_{\text{meso}\leftrightarrow\text{micro},j}(u)$, to account for the spectral content of the scales-interactions. Then, Eq. (5) breaks down the total spectral contribution $\mathbf{S}_j(u)$ into three distinct terms. The first term, $\mathbf{S}_{\text{micro},j}(u)$, relates to a stationary and isotropic turbulence (Vercauteren et al. 2019); critical to calculate the microscale flux (Arya and Holton 2001). However, over time, the precision of flux calculation is affected by the presence of nonstationary components. The second term represents such components, $\mathbf{S}_{\text{meso},j}(u)$, which are associated with mesoscale fields. Also, it is possible to observe changes in the fluxes due to bidirectional scale interactions—mesoscale motions into microscale or the opposite. Therefore, the third term, $\mathbf{S}_{\text{meso}\leftrightarrow\text{micro},j}(u)$, accounts for the interaction between microscale and mesoscale processes (Kang 2009). However, since

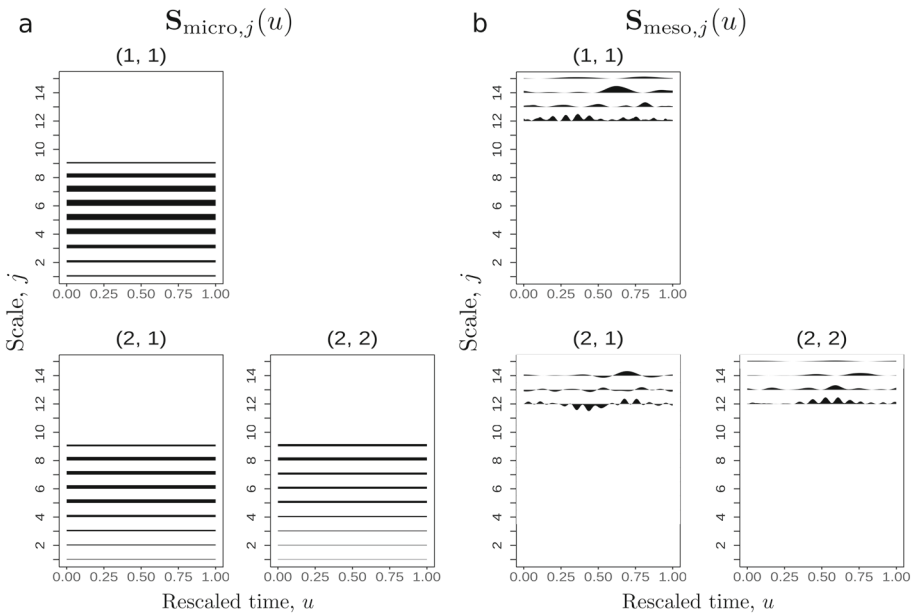

Fig. 1 The LWS matrix $\mathbf{S}_j(u)$ contains two contributions: **a** the stationary microscale $\mathbf{S}_{\text{micro},j}(u)$ and **b** the nonstationary mesoscale $\mathbf{S}_{\text{meso},j}(u)$. The indexes (p, q) are indicated above each panel. Values of $\mathbf{S}_{\text{meso},j}(u)$ were scaled to enhance shape details

our focus is on fluxes during a limited-time interaction, the third term, $\mathbf{S}_{\text{meso}\leftrightarrow\text{micro},j}(u)$, is considered negligible. This assumption implies that the spectral gap exist in the spectrum $\mathbf{S}_j(u)$ in Eq. (5) and that the microscale component $\mathbf{S}_{\text{micro},j}(u)$ can be estimated accurately.

Under this general model, we aim to simulate a bivariate ($P = 2$) turbulent time series, e.g., w' and T_s', with spectral and cospectral characteristics established as defined by $\mathbf{S}_j(u) = \mathbf{S}_{\text{micro},j}(u) + \mathbf{S}_{\text{meso},j}(u)$. To achieve this, we propose a 2×2 LWS matrix $\mathbf{S}_j(u)$ (i.e., $p, q \in \{1, 2\}$) with $J = 15$ scales, resulting in a bivariate time series of approximately one hour with a frequency of 10 Hz. Figure 1 presents the microscale $\mathbf{S}_{\text{micro},j}(u)$ (Fig. 1a) and mesoscale $\mathbf{S}_{\text{meso},j}(u)$ (Fig. 1b) of the LWS matrix $\mathbf{S}_j(u)$.

The stationary microscale contribution $\mathbf{S}_{\text{micro},j}(u)$ (Fig. 1a) follows spectral power laws in specific timescales as defined by Kaimal and Finnigan (1994) and Katul and Chu (1998). The dependence of the elements $S^{(p,q)}_{\text{micro},j}(u)$ on the average atmospheric timescale τ_j and on the exponent α_j is illustrated in Eq. (6):

$$S^{(p,q)}_{\text{micro},j}(u) = A^{(p,q)}_j \tau_j^{-\alpha_j - 1}. \tag{6}$$

The parameter $A^{(p,q)}_j$ is a proportional constant for the spectrum ($p = q$) and the cospectrum ($p \neq q$) at scale j. At the same time, the dimensionless value α_j is linked to a spectrum power law (Percival 1995). The parameter values used in this work are outlined in Table 1. The values of $A^{(p,q)}_j$ were chosen to ensure obtaining realistic fluxes based on field experiments (Ortiz et al. 2019; Morales 2020). As for α_j values, Kaimal and Finnigan (1994) approximated the microscale spectrum for low frequencies, $f \to 0$ (i.e., $\tau \to \infty$), as a constant ($\alpha_j = 0$). However, Katul and Chu (1998) found that a power law with $\alpha_j = -1$ is suitable for frequency bands associated with turbulence production range. Similarly, $\alpha_j = -5/3$

Table 1 Parameters for the theoretical spectrum ($p = q$) and cospectrum ($p \neq q$) elements $S^{(p,q)}_{\text{micro},j}(u)$ use in Eq. (6)

Element	Scale (j)	$A_j^{(p,q)}$	Power law (α_j)
$S^{(1,1)}_{\text{micro},j}$	1 to 5	1×10^{-3}	$-5/3$
	6 to 7	$\approx 2.845 \times 10^{-3}$	-1
	8 and 9	$\approx 1.094 \times 10^{-1}$	0
	10 to 15	0	–
$S^{(2,1)}_{\text{micro},j}$	1 to 5	2×10^{-3}	$-5/3$
	6 to 7	$\approx 5.691 \times 10^{-3}$	-1
	8 and 9	$\approx 2.188 \times 10^{-1}$	0
	10 to 15	0	–
$S^{(2,2)}_{\text{micro},j}$	1 to 4	5×10^{-3}	$-5/3$
	5 and 6	$\approx 8.963 \times 10^{-3}$	-1
	7 and 8	$\approx 1.720 \times 10^{-1}$	0
	9 to 15	0	–

denotes the inertial range of Kolmogorov's power law at high frequencies. Furthermore, the average atmospheric timescale in seconds can be expressed in terms of the scale j and the instrumental sampling rate f—see Eq. (7):

$$\tau_j = \frac{1}{2f}(2^j + 2^{j+1}). \tag{7}$$

For instance, using the distributive property for f, we obtain the terms $2^j/f$ and $2^{j+1}/f$. Then, consider $j = 1$—the finest scale of $\mathbf{S}_j(u)$—and $f = 10$ Hz. The first term yields 0.2 s—the timescale related to the Nyquist frequency $f/2 = 5$ Hz—and the second, 0.4 s. The values 0.2 s and 0.4 s are the lower and upper timescales for the bandwidth associated with the scale $j = 1$. Adding and dividing these values in two, we obtain 0.3 s, the average atmospheric timescale for $j = 1$.

The mesoscale contribution $\mathbf{S}_{\text{meso},j}(u)$ (Fig. 1b) was chosen through spectral and cospectral estimations of experimental data that was collected in Bogota, Colombia during a measurement campaign in 2019 (Ortiz et al. 2019). The region has a weak wind regime and a heterogeneous topography that caused nonstationary records due to local circulations, as defined by the Foken and Wichura (1996) test. The nonstationary character is shown as wave-like motions with amplitude-modulated and time-varying frequencies, like the so-called "dirty" waves (Nappo et al. 2014). To account for this nonstationarity in our simulation, low-frequency contributions were extracted from the LWS matrix estimations of the experimental data and added to the theoretical spectrum at scales $j \in \mathbb{N}_{12}^{15}$. This ensured that the theoretical spectrum and cospectrum exhibited nonstationary behavior, as outlined in Eq. (5). The mesoscale contribution $\mathbf{S}_{\text{meso},j}(u)$ was about ten times larger than $\mathbf{S}_{\text{micro},j}(u)$, with a spectral gap separating them at $j \in \{10, 11\}$.

3.2 Assessment of Stationary and Nonstationary Fluxes Using Synthetic Signals

From a specific time-dependent spectrum and cospectrum matrix, e.g., $\mathbf{S}_j(u)$, we can simulate signals using the framework proposed by Park et al. (2014). For further details on simulation

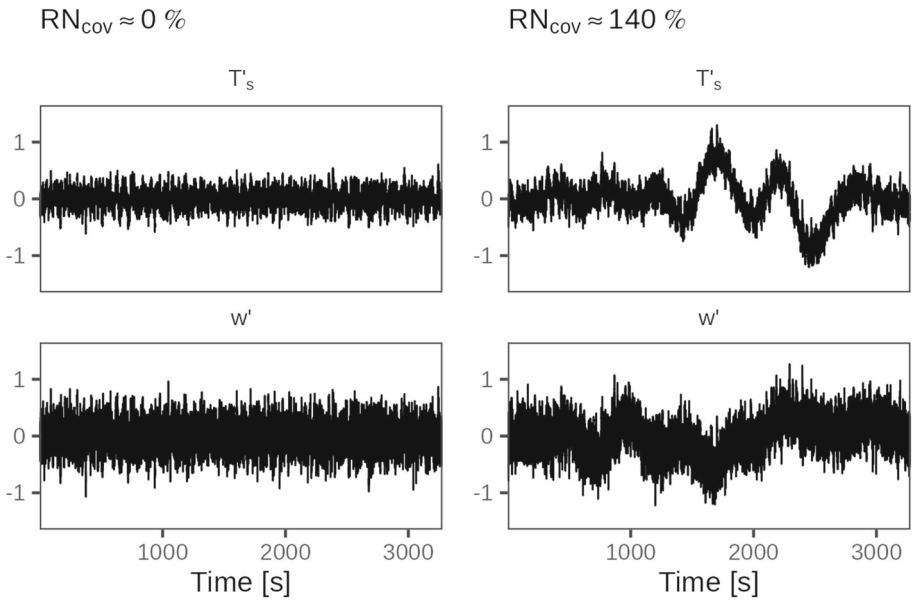

Fig. 2 Two realizations of a bivariate LSW process: **a** stationary with $\mathbf{S}_{\text{micro},j}(u)$ and **b** nonstationary with $\mathbf{S}_j(u)$

Table 2 Summary of RN_{cov} from simulation

Spectrum	Mean	Sta. Dev.	Min.	Q_1	Median	Q_3	Max.
$\mathbf{S}_{\text{micro},j}(u)$ $(\times 10^{-2})$	1.1	1.0	0.0	0.6	1.0	1.4	9.5
$\mathbf{S}_j(u)$	348.7	1619.6	0.14	14.8	39.0	77.3	18,078.9

The values in the table are in percentages (%)

using the mvLSW R-package see Taylor et al. (2019, 2022). This method allows generating two simulation cases: one where the contribution is stationary, provided by $\mathbf{S}_{\text{micro},j}(u)$, and another where the contribution is nonstationary, provided by $\mathbf{S}_j(u)$. For each case, we simulate 200 bivariate time series of length $T = 32{,}768$ (i.e., $J = 15$) with Gaussian innovations and a least asymmetric Daubechies wavelet of support $N = 10$. The bivariate time series is equivalent to a record of two turbulence signals, such as (w', T_s'), sampled at 10 Hz with a duration of 54.6 min.

Figure 2 displays a realization of these simulations and shows the value of the steadiness test of Foken and Wichura (1996). We denote the value of the steadiness test by RN_{cov}—according to Foken et al. (2005)—where $\text{RN}_{\text{cov}} > 30\%$ indicates a nonstationary flux measurement (Foken and Wichura 1996; Foken et al. 2005). The Fig. 2 presents a stationary case with $\text{RN}_{\text{cov}} \approx 0\%$ (Fig 2a) and a nonstationary case with $\text{RN}_{\text{cov}} \approx 140\%$ (Fig 2b)—these last records must be flagged as part of quality assessment for the eddy-covariance technique (Foken and Wichura 1996; Foken et al. 2005). In this line, the RN_{cov} value measures roughly the level of nonstationarity of the atmospheric flow, as we can note in the statistic summary shown in the Table 2, time-varying cospectrum links to high RN_{cov} values.

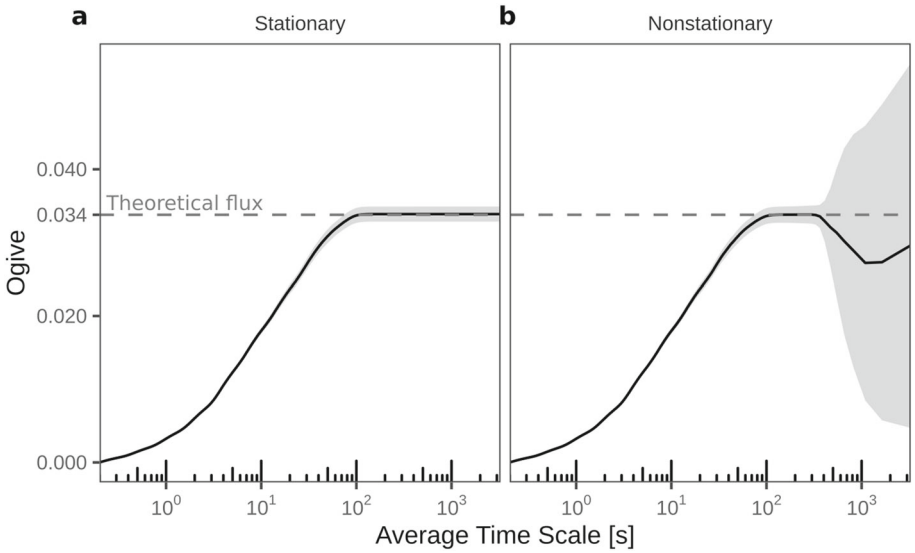

Fig. 3 Ogive function in **a** stationary and **b** nonstationary conditions. Black lines depict the mean ogive function, and shaded areas show one standard deviation

Table 2 summarizes $\mathrm{RN}_{\mathrm{cov}}$ values for synthetic signals for both $\mathbf{S}_{\mathrm{micro},j}(u)$ and $\mathbf{S}_j(u)$ spectra. Here, we outline the mean, standard deviation, minimum, first quartile (Q_1), median, third quartile (Q_3), and maximum for $\mathrm{RN}_{\mathrm{cov}}$ values. For $\mathbf{S}_{\mathrm{micro},j}(u)$, the $\mathrm{RN}_{\mathrm{cov}}$ values are low, with mean of $1.1 \times 10^{-2}\%$ and standard deviation of $1.0 \times 10^{-2}\%$, indicating a generally stationary condition which implies an accurate estimate of fluxes. In contrast, $\mathbf{S}_j(u)$ shows higher and more variable $\mathrm{RN}_{\mathrm{cov}}$ values, with a mean of 348.7% and standard deviation of 1,619.6%, these results suggest a nonstationary condition. Furthermore, the median value for $\mathbf{S}_j(u)$ is 39.0%, indicating that these simulated fluxes exceed the threshold established by Foken and Wichura (1996).

On the other hand, Fig. 3 shows the ogive function for stationary (panel left) and nonstationary (panel right) conditions. The horizontal axis is the average atmospheric timescale τ, and the vertical axis is the cumulative cospectrum. The black line is the mean ogive from simulations, and the shaded area around this mean is a range defined as one standard deviation from the mean. The dashed horizontal line is the stationary theoretical flux with a value of $\langle c^{(2,1)} \rangle_{\mathrm{theoretical}} = 0.034$ based on $\mathbf{S}_{\mathrm{micro},j}(u)$.

For the stationary scenario depicted by $\mathbf{S}_{\mathrm{micro},j}(u)$, the ogive function converges toward the theoretical flux line (Fig. 3a). Such convergence, at larger average timescales, is typical of stationary conditions. The narrow shaded region indicates a precise flux estimation. Conversely, the nonstationary case from $\mathbf{S}_j(u)$ (Fig. 3b) diverges from the theoretical flux exhibiting significant variability at larger timescales. This is highlighted by the broad shaded region. This variability stems from the poor sampled cospectral contribution at scales $j \in \mathbb{N}_{12}^{15}$ and provides an unreliable flux estimation.

Here, we simulated atmospheric turbulence signals using the mvLSW framework under stationary and nonstationary conditions. These conditions are supported by statistical analysis of $\mathrm{RN}_{\mathrm{cov}}$ (Table 2) and the ogives test (Fig. 3). In the next section, we demonstrate how the cross-covariance signal $c^{(p,q)}(u, 0)$, defined by the LWS spectrum $\mathbf{S}_j(u)$, can visualize the stationary and nonstationary behavior in the turbulent flux.

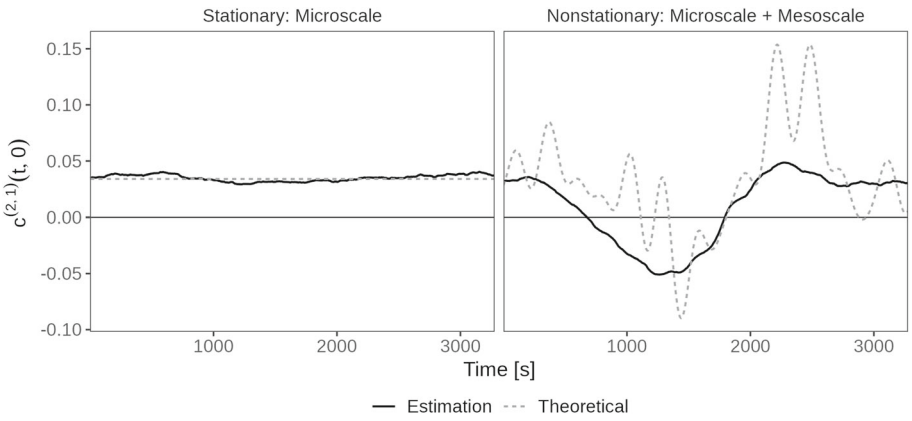

Fig. 4 Comparison of local flux signals for both stationary (left panel) and nonstationary (right panel) cases. The black solid lines represent the estimations and the grey dashed lines are their theoretical versions

3.3 Local Covariance and Cross-Covariance in Atmospheric Fluxes

In Sect. 2, the local covariance and cross-covariance signal $c^{(p,q)}(u, \tau)$ is defined using the LWS matrix $\mathbf{S}_j(u)$ (see Eq. (3)). The cross-covariance signal measures the interdependence between two signals across time and scale. In the case of turbulence time series, the local cross-covariance at $\tau = 0$, $c^{(p,q)}(u, 0)$ with $p \neq q$ can be thought of as a local atmospheric flux in kinematics units. This local flux measures the mean flux at the normalized time interval $(u, u + \delta u)$. Following Nason et al. (2000), under stationary conditions, this time-dependent flux converges to the total integrated atmospheric flux for the measured period and equals the flux obtained by the eddy-covariance method.

In Fig. 4, we compared the local flux signals denoted by $c^{(2,1)}(t, 0)$ for the realizations shown in Fig. 2 and its theoretical version defined by $S^{(2,1)}_{\text{micro},j}(u)$ and $S^{(2,1)}_j(u)$, for both stationary (left panel) and nonstationary (right panel) cases. The black solid line represents the estimated local flux signal for both realizations of Fig. 2—for the realizations, first, we estimate the LWS matrix, then, we reconstruct the flux signal with Eq. (3)—and the grey dashed line represents the theoretical reconstruction based on the theoretical $S^{(2,1)}_{\text{micro},j}(u)$ and $S^{(2,1)}_j(u)$—see Fig. 1 and Eq. (5).

In the stationary case, the local flux signal remains constant, converging to a total integrated atmospheric flux given by the theoretical value of $\langle c^{(1,2)} \rangle_{\text{theoretical}} = 0.034$ based on $\mathbf{S}_{\text{micro},j}(u)$. The estimated signal closely matches the theoretical value with a root mean square error (RMSE) of $\text{RMSE}_{\text{micro}} = 0.003$. On the other hand, in the nonstationary case, the local flux exhibits erratic patterns due to large-scale components integrating the cospectrum, $S^{(2,1)}_{\text{meso},j}(u)$ contained in $S^{(2,1)}_j(u)$. Here, estimating local flux is challenging due to the difficulty in determining the coarse-scale of the cospectrum, as seen in the difference between the estimated signal (black line) and its theoretical (dashed grey line)—see the panel on the right of Fig. 4. The RMSE value supports this for the nonstationary case is $\text{RMSE}_{\text{meso}} = 0.042$, which is one order of magnitude higher than $\text{RMSE}_{\text{micro}}$.

This analysis shows that the nonstationary atmospheric flux can be visually assessed through the local flux signal, denoted by $c^{(2,1)}(t, 0)$. The time pattern of the flux signal is determined by the spectral representation $S^{(2,1)}_j(u)$, making it an effective way to detect

nonstationary features. In our simulation, the nonstationary behavior is due to mesoscale motion. However, this local flux signal can also indicate the presence of nonstationary features due to other types of atmospheric phenomena, such as nonstationary motions present in the microscale, including for example coherent structures. At this point, it is important to distinguish the contributions to the atmospheric flow from the various atmospheric phenomena that may be present in the airflow. In the case of signals contaminated by mesoscale motion, we need to identify a specific scale between mesoscale and microscale, commonly called the spectral gap.

3.4 Local Detection of the Spectral Gap

Accurate estimations of the atmospheric flux involve separating the stationary component of the flux commonly associated with the microscale motion from the mesoscale motions. This separation can be achieved by identifying a region of low cospectral intensity related to turbulent fluxes, also known as a cospectral gap (Stull 1988; Vickers and Mahrt 2003; Voronovich and Kiely 2007; Babić et al. 2017; Lehner and Rotach 2023). Here, we propose a method for detecting the cospectral gap that relies on the time-varying features of $\mathbf{S}_j(u)$ and adapts the ideas presented by Voronovich and Kiely (2007).

To accomplish this, we define a grid of equally spaced normalized time instants denoted by $u_i \in \{u_1, u_2, \ldots\}$—the grid spans signal duration. Then, to each u_i, we fit a fifth-order polynomial $P_i(j)$ across scale j by a least-squares technique—as suggested by Voronovich and Kiely (2007), Babić et al. (2017) and Lehner and Rotach (2023)—to the cospectrum elements $S_j^{(2,1)}(u_i)$, elements associated with the turbulent flux. As described in Voronovich and Kiely (2007) and Babić et al. (2017), we apply a set of rules and goodness of fit conditions to detect the local spectral gap $j_{g,i}$ at each u_i. The set rules for each u_i are:

1. $P_i(j)$ was checked for an local extremum E_0 in a region defined by the timescale $\tau_j = \tau_{E_0} < 200$ s;
2. $P_i(j)$ was checked for critical points as roots, R_i, extrema, E_i and inflection points, I_i (with $I_1 < I_2 < \ldots$), at the region $\tau_{E_0} < \tau_j < T$, where $T = 2^J/f$, where f is in Hz, represents the signal duration in seconds. For instance, in the case of $J = 14$ and $J = 15$, and frequency sampling at 10 Hz, we get $T \approx 27.3$ min and $T \approx 54.6$ min, respectively;
3. The derivative at $j = I_2$ was checked to be small $|P'(I_2)/P'(I_1)| < 0.5$. If this condition is satisfied, I_2 can be accepted as the gap scale;
4. The gap scale $j_{g,i}$ can be found from $P_i(j_{g,i}) = P_i(j_m) + 0.02\,[P_i(E_0) - P_i(j_m)]$, where $j_m = \min\{E_1, R_1, I_2\}$.

The timescales τ_j and τ_{E_0} are related to j and E_0 using Eq. (7). The goodness of fit conditions ensures that the estimated local spectral gap $j_{g,i}$ is derived from polynomial fits that explain the spectrum and cospectrum at u_i. Therefore, we use the $P_i(j)$ that satisfy the next condition:

$$\epsilon = \frac{\sum_{j=1}^{J}\left[P_i(j) - S_j^{(2,1)}(u_i)\right]^2}{\sum_{j=1}^{J}\left[S_j^{(2,1)}(u_i) - \langle S^{(2,1)}(u_i)\rangle\right]^2} \leq 0.25 : \tag{8}$$

where $\langle S^{(2,1)}(u_i)\rangle$ is the arithmetic mean of $S_j^{(2,1)}(u_i)$ and J the coarsest scale. Based on the multiple estimations $j_{g,i}$ for the bivariate turbulent signals $\mathbf{X}_{t;T}$, we define the mean function

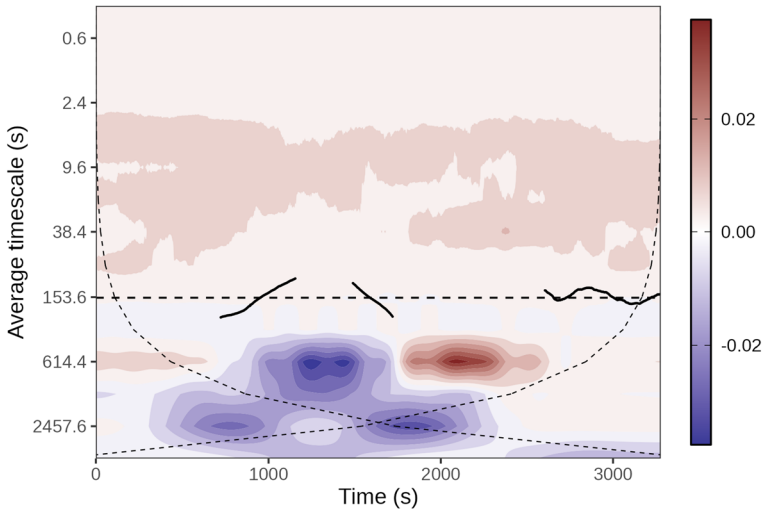

Fig. 5 Cospectrum $S_j^{(2,1)}(u)$ across time and scale. The black points indicate local estimations of the cospectral gap $j_{g,i}$, and the dashed line is the mean cospectral gap j_g

j_g and the variance Δj_g^2 of the cospectral gap as,

$$j_g = \mathrm{E}[j_{g,i}]: \tag{9}$$

$$\Delta j_g^2 = \mathrm{E}[(j_{g,i} - j_g)^2] = \mathrm{var}(j_{g,i}). \tag{10}$$

where E denotes the expected value operator.

Figure 5 display the cospectrum $S_j^{(2,1)}(u)$ for nonstationary realizations (Fig. 2b). The cospectrum measures the interdependence between turbulent signals across time (x-axis) and average timescale (y-axis), where this average timescale, τ_j, is related to the scale, j by Eq. (7). In the cospectrum, red tones indicate positive correlations, while blue tones indicate negative correlations. Also, local estimations of cospectral gap $j_{g,i}$ are represented by black points. The mean function j_g—estimated as the arithmetic average—is depicted by a dashed black line, and the cone of influence is represented by the curve-dashed line.

Depending on the average timescales, the cospectrum of the surface fluxes displays two separate regions. A stationary region with a homogenous surface that remains constant over time ($0.3\ \mathrm{s} \leq \tau_j \leq 153.6\ \mathrm{s}$). And a heterogenous surface ($\tau_j > 153.6$ s), with time-varying features and poor intensity estimations, implying a nonstationary behavior. The black points are located between the two regions, effectively separating them. In this example, we cannot detect the cospectral gap at each point in time, which is 500 equally spaced time points, because it does not meet the conditions of the polynomial fit (Voronovich and Kiely 2007). However, successful local detections seem to be concentrated on a single cospectral gap. Then, we obtain the mean cospectral gap at the average timescale $\tau_{j_g} = 158.6 \pm 31.8$ s (arithmetic mean $\pm$ one standard deviation) for the nonstationary realization. Using Eq. (7), we determined that this timescale corresponds to a scale $j_g = 10.0 \pm 0.3$, with $\Delta j_g = 0.3$, which corresponds to the theoretical gap defined by $\mathbf{S}_j(u)$—for details, see Sect. 3.1.

With the cospectral gap defined, we can calculate the surface flux for the microscale contribution. To achieve this, we reconstruct the band-limited covariance signal $c_{1,j_g}^{(2,1)}(u, 0)$ with $m_0 = 1$ and $m = j_g$ (Eq. 3). In this example, the covariance signal displays similar

behavior to the stationary case shown by the solid black line in Fig. 4. Finally, using Eq. (4), we obtain a microscale flux $\langle c_{1,j_g}^{(2,1)} \rangle = 0.035$, with $\sim 3\%$ relative difference from the theoretical value.

Moreover, by analyzing the time-varying cospectrum $S_j^{(2,1)}(u)$, we can estimate the cospectral gap locally. These local detections allow us to evaluate the statistical properties of the cospectral gap and assess its stability over time and convergence on a specific timescale.

4 Application

4.1 Selection and Preprocessing of Turbulence Time Series

In this section, we apply the mvLSW approach to estimate turbulent heat fluxes under nonstationary conditions in two distinct regions: Fairbanks, Alaska, and Bogota, Colombia. Fairbanks is located in the Interior of Alaska region, a high-latitude area at (64°49'N and 147°52'W). During winter, the surface energy balance is primarily dominated by surface radiative cooling; this forcing mechanism initiates the formation of a stably stratified atmospheric boundary layer (ABL) (Malingowski et al. 2014; Fochesatto et al. 2015). Due to the Fairbank's topographic features, the stratified ABL is often influenced by shallow cold flows, a mesoscale motion (Mayfield and Fochesatto 2013; Fochesatto et al. 2015). On the other hand, Bogota is located in the eastern trifurcation of the Andes at 4°36'N latitude and 73°4'W longitude, a tropical megacity (Ortiz et al. 2019). Its atmospheric conditions are mainly driven by convection, while the urban canopy shapes air masses at the regional level. Such atmospheric and topographic conditions suggest that the ABL can be affected by mesoscale motions induced by anabatic-katabatic winds and landscape channeling (Guerrero and Jimenez 2014; Ortiz et al. 2019).

In both locations, Fairbanks and Bogota, we collected measurements of the three velocity components (u, v, w) and sonic temperature (T_s) using sonic anemometers set on eddy-covariance towers. Both anemometers sample at 10 Hz with a resolution of 0.01 m s^{-1}. In the case of Fairbanks, turbulent measurements were taken with the 3D sonic anemometer CSAT3 installed at a 3 m tower at UAF-Farm under the ALPACA project (Simpson et al. 2024). In the case of Bogota, turbulent measurements were taken with the 3D sonic anemometer Windmaster Pro 3D installed at a 10 m tower at Parque Simon Bolivar (Ortiz et al. 2019).

Datasets collected in both sites, Fairbanks and Bogota, have been despiked according to Starkenburg et al. (2016). A spike count less than 1% was ensured for the selected time series. Also, we verified that measurements were not flagged by instrumental issues such as amplitude resolution, dropouts, and discontinuities (Vickers and Mahrt 1997). To avoid nonstationary behavior caused by changes in wind direction during the measurement period, we calculated wind direction in $N = 30$ segments and quantified its variability. Per segment, we calculated $\theta_i = \tan^{-1}(\bar{v}_i \cdot \bar{u}_i^{-1})$ for $i = 1, \ldots, 30$, where $\bar{v}_i$ and $\bar{u}_i$ are the average crosswind components for the segment i. Now, defining the mean wind direction as $\bar{\theta} = N^{-1} \sum_{i=1}^{N} \theta_i$ and standard deviation $s_\theta = \sqrt{(N-1)^{-1} \sum_{i=1}^{N} (\theta_i - \bar{\theta})^2}$, we calculated the coefficient variation as $\mathrm{CV}_\theta = s_\theta \bar{\theta}^{-1}$, choosing signals that $\mathrm{CV}_\theta < 0.2$. Finally, with these considerations, we selected the records where the value of the Foken and Wichura (1996) test exceeds the threshold $\mathrm{RN}_{\mathrm{cov}} > 30\%$. Specifically, for Fairbanks heat flux (i.e., $\overline{w'T_s'}$), $\mathrm{RN}_{\mathrm{cov}} \approx 20{,}000\%$ and for Bogota heat flux, $\mathrm{RN}_{\mathrm{cov}} \approx 200\%$.

In the Fairbanks datasets, we analyzed a nonstationary turbulence record during the winter season—27.3 min, i.e., 2^{14} observations—from February 24, 2023, starting at 00:00 h. The measurements were obtained under stable conditions, where the presence of shallow cold flows (Fochesatto et al. 2015) can considerably affect turbulent heat fluxes (Maillard et al. 2022; Simpson et al. 2024). Similarly, in Bogotas' datasets, we studied a nonstationary record during the winter (i.e., rainy season)—54.6 min, i.e., 2^{15} observations—from October 9, 2014, starting at 12:00. The atmospheric conditions during the observations indicate unstable conditions in the surface layer with some radiation interruption by cloudiness. The observational site is at the Parque Simon Bolivar in downtown Bogota. This site reflects fluxes from a typical urban canopy where green spaces are surrounded by large buildings and structures (Ortiz et al. 2019). Therefore, given the case of two very different atmospheric conditions, we have chosen to process time series length $\sim$ 30 min and $\sim$ 60 min. In both cases, it was possible to detect the spectral gap successfully. However, it must be noted that the search and successful estimation requires an adequate low-frequency sampling strategy that is limited by the evaluated time frame. This is why this estimation falls outside the 95% level of confidence when the time series are length-limited.

4.2 Results and Discussions

In Fig. 6, we show the cospectrum $S_j^{(2,1)}(t)$ (left panels) and local flux $c^{(2,1)}(t,0)$ (right panels) for Fairbanks (upper panels) and Bogota (lower panels) used to estimate the microscale flux. On the left, the cospectrum $S_j^{(2,1)}(t)$ displays local cospectral gaps $j_{g,i}$, the average cospectral gap j_g, and the cone of influence—indicated by black points, horizontal long-dashed and short-dashed lines, each. On the right, the local flux $c^{(2,1)}(t,0)$ includes its band-limited $c_{1,j_g}^{(2,1)}(t,0)$ and full $c_{1,J}^{(2,1)}(t,0)$ reconstruction (microscale and full contribution, each), and the eddy covariance estimation F_{EC}—via black solid, dark grey short-dashed and light grey long-dashed lines, respectively.

In both sites, the cospectral gaps are $\tau_{j_g} = 259 \pm 203$ s for Fairbanks and $\tau_{j_g} = 710 \pm 240$ s for Bogota, suggesting smaller eddy sizes in Fairbanks's microscale turbulence compared to Bogota. This difference is due to the atmospheric conditions being very stable in Fairbanks ($L^* = 8.0$ m, in terms of the Obukhov length) and unstable in Bogota ($L^* = -2.5$ m). These results are consistent with previous research. For instance, in stable conditions, Vickers and Mahrt (2003) reports timescale gaps of 30 s, approximating the lower bound of the spectral gap in Fairbanks at 56 s. Voronovich and Kiely (2007) reports timescale gaps between 330 s and 800 s, which approximates the upper bound of which approximates the upper bound of 462 s at Fairbanks. On the other hand, for daytime, Babić et al. (2017) reports spectral gaps of 1020 s and 1740 s, and Donateo et al. (2017) reports scale gaps of 1800 s for daytime. These values are larger than the upper bound of the spectral gap for Bogota, $\sim$ 960 s. However, measurements in Bogota were made during the winter season affected by high cloud coverage and rain. In Fig. 6a, c, for both locations, the cospectral gap τ_{j_g} split $S_j^{(2,1)}(t)$ in two cospectral regions—fine and coarse scales regions. The fine-scale cospectral regions, for Fairbanks ($\tau_{j_g} < 259$ s) and Bogota ($\tau_{j_g} < 710$ s), are roughly time-invariant, as expected for the microscale; the coarse-scale cospectral region, for Fairbanks ($\tau_{j_g} > 259$ s) and Bogota ($\tau_{j_g} > 710$ s), exhibits time-localized perturbations, caused by low-frequency wind motions.

Then, in Fig. 6b, d, we note that mesoscale wind motions offsets and distort microscale local flux signal—the full cross-covariance signal $c_{1,J}^{(2,1)}(t,0)$ is, essentially, a shifted version of $c_{1,j_g}^{(2,1)}(t,0)$. These low-frequency motions, combined with the high uncertainty affecting

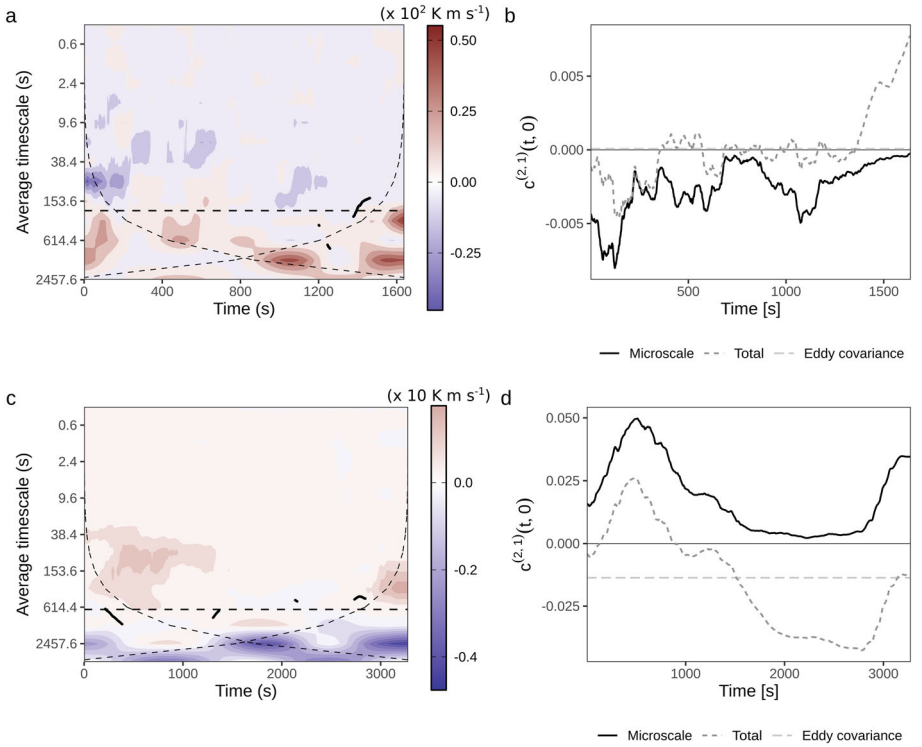

Fig. 6 On the left, we show the kinematic heat cospectrum for **a** Fairbanks (upper) and **c** Bogota (lower), with black points indicating the local cospectral gaps $j_{g,i}$ and a dashed line representing the mean cospectral gap j_g. On the right, local flux signals $c^{(2,1)}(t, 0)$ for **b** Fairbanks (upper) and **d** Bogota (lower) are depicted using solid black lines for bandwidth-limited flux and dashed dark gray lines for the full signal flux. The dashed light grey line is the eddy-covariance flux

local flux signal estimates, obscure the interpretation of the microscale contributions. This is reflected when comparing the integrated total and the eddy-covariance fluxes against the band-limited integrated flux (i.e., using the cospectral gap j_g). In Fairbanks, the integrated total flux $\langle c^{(2,1)} \rangle_{\text{Total}} = 0.05 \times 10^{-3}$ K m s^{-1} and eddy-covariance flux $\text{F}_{\text{EC}} = 0.09 \times 10^{-3}$ K m s^{-1} indicate a positive kinematic flux. But, when comparing to the reconstructed microscale flux, $\langle c^{(2,1)} \rangle_{\text{Microscale}} = -1.26 \times 10^{-3}$ K m s^{-1}, a higher heat flux follows more closely the radiative cooling process and help closing the energy balance (Maillard et al. 2022).

Conversely, in Bogota, the total integrated flux $\langle c^{(2,1)} \rangle_{\text{Total}} = -14.9 \times 10^{-3}$ K m s^{-1} and the eddy-covariance flux $\text{F}_{\text{EC}} = -13.6 \times 10^{-3}$ K m s^{-1} implying a stable condition. But, integrating the microscale flux, $\langle c^{(2,1)} \rangle_{\text{Microscale}} = 18.4 \times 10^{-3}$ K m s^{-1}, reflects that, effectively, the flux is positive. This significant difference in the flux estimation is attributed to a large reduction in solar radiation due to increasing cloudiness at the time of the observations. This meteorological feature introduces a negative trend in the air temperature. However, it must be noted here that in that observational site a plausible interpretation of negative fluxes could be hypothetically verified if precipitation events were to precede the time series (e.g., surface cold pools).

Using the mvLSW approach, both the cospectrum $S_j^{(2,1)}(t)$ and the local flux signal $c^{(2,1)}(t,0)$ are crucial in visualizing and interpreting the impact of mesoscale wind motions on microscale turbulence—as we demonstrate by comparing the band-limited local flux signal $c_{1,j_g}^{(2,1)}(t,0)$ with its full reconstruction $c_{1,J}^{(2,1)}(t,0)$. Despite assuming stationary microscale conditions and the presence of a spectral gap for this study, real-world applications (see Fig. 6) often challenge these assumptions. Figure 6b, d illustrate that microscale signals can exhibit temporal variations. At times, it may be challenging to separate between mesoscale motions and microscale turbulence, indicating a possible significant time-localized interaction component. Nonetheless, this work provides a step forward in employing the mvLSW model to analyze surface turbulence flux within increasingly complex surface and atmospheric flow scenarios.

5 Conclusions

This study introduces the mvLSW model as a theoretical framework for analyzing turbulence fluxes under complex atmospheric and surface conditions. Specifically, we simulate a scenario where mesoscale wind motions impact the stationary microscale turbulence. Through this simulation, we generated a synthetic time series providing stationary and nonstationary turbulence conditions. This was achieved employing theoretical spectrum and cospectrum—a theoretical LSW matrix—that replicates these scenarios. For the nonstationary case, we split the cospectral components associated with the mesoscale and microscale, adapting the Voronovich and Kiely (2007) algorithm for gap detection to the time-variant cospectrum. Based on this method, we identify the spectral gap locally in time, allowing us to investigate its statistical properties and time-variant behavior. Although this simulation study assumes microscale stationarity and the presence of a spectral gap, the mvLSW model is adaptable to other complex case studies through accurate spectral modeling. Such case studies can include nonstationary microscale phenomena e.g., intermittent turbulence, coherent structures, and conditions where local and regional winds affect turbulence flux. Also, this methodology can potentially be used to analyze airborne collected turbulence flux measurements, where air masses with different scales of motion are recorded in short periods of time (Strunin and Hiyama 2004). Finally, the mvLSW methodology seems effective in examining complex atmospheric conditions where surface turbulent fluxes are affected by scale-dependent atmospheric forcing (see Sect. 4 and "Appendix 1"). Further applications can be envisioned using the statistical modeling methodology to introduce a specific atmospheric scale forcing and compare the model with experimental data. Overall, these findings underscore the importance of considering scale-atmospheric forcing when computing turbulent fluxes and compare them with high resolution model outputs.

Appendix 1: Momentum Turbulent Fluxes

Following Sect. 4, this appendix presents the analysis of the momentum turbulent fluxes, specifically for Fairbanks. Figure 7 shows the spectrum and cospectrum of u', v', w', $u'v'$, $u'w'$ and $v'w'$. We note that the spectral gap for most of the variances and cross-covariances occurs around the average timescale of $\tau_g \sim 300\,\mathrm{s}$, except for the cospectrum $u'v'$, which occurs around $\tau_g \sim 150\,\mathrm{s}$. This is important because it describes a mesoscale perturbation

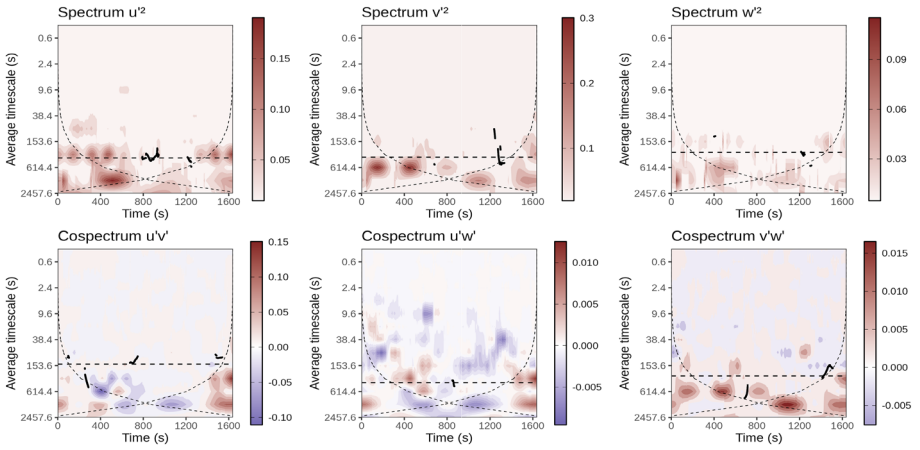

Fig. 7 Spectrum of the turbulent velocity fields (u', v', w'). The upper panels are the spectrum components $S_j^{(u',u')}(t)$, $S_j^{(v',v')}(t)$ and $S_j^{(w',w')}(t)$. The bottom panels are the spectrum components $S_j^{(u',v')}(t)$, $S_j^{(u',w')}(t)$ and $S_j^{(v',w')}(t)$. The x-axis indicates the time in seconds; the y-axis is the average timescale τ_j related to the timescale bandwidth associated with the scale j. The black points mark local cospectral gaps $j_{g,i}$, and a dashed line represents the mean cospectral gap j_g for the spectrum and cospectrum

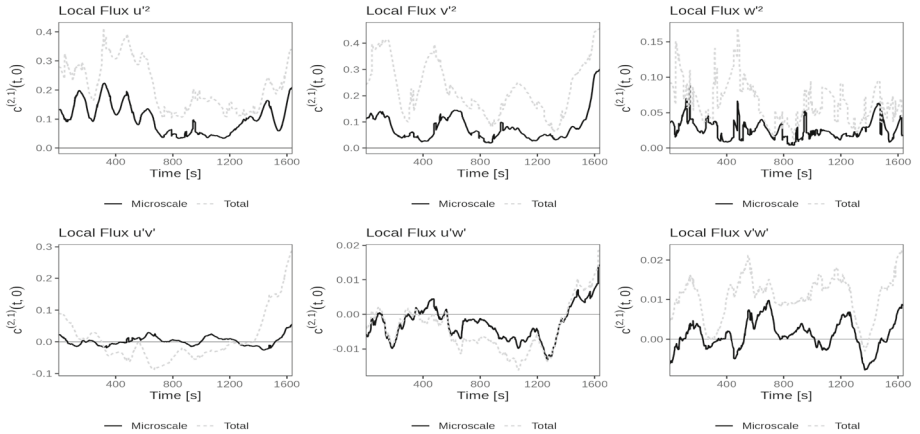

Fig. 8 Local variance and cross-covariance of the turbulent velocity field (u', v', w'). The upper panels are the local variances $c^{(u',u')}(t,0)$, $c^{(v',v')}(t,0)$ and $c^{(w',w')}(t,0)$. The bottom panels are the cross-covariance $c^{(u',v')}(t,0)$, $c^{(u',w')}(t,0)$ and $c^{(v',w')}(t,0)$. The x-axis indicates the time in seconds; the y-axis is the strength of the dependence. For each case, it is shown the local variance and cross-covariance, fully reconstructed (dashed gray line) and partially reconstructed (solid black line)—we referenced as a partial reconstruction when the local cross-variance is reconstructed from the finest scale $m_0 = 1$ to the spectral gap $m = j_g$

spread across all fields. However, it must be clarified that not all fields are expected to be perturbed simultaneously.

Similarly, and based on the results of Fig. 7, Fig. 8 presents the time series of the reconstructed of u', v', w', $u'v'$, $u'w'$ and $v'w'$ momentum fluxes. Here, we note a clear difference between the total and microscale flux across all variables. In these cases, the time series were computed using the time-averaged spectral gap found and indicated in the dashed line in

Fig. 7. Such difference relates to the existing energy in the cross-spectrum (see Fig. 7) at low frequencies.

Acknowledgements The authors acknowledge the support from the Universidad del Valle Sede Cali under the research grants code CI-21134, 124-2020 and MInCiencias (Colombia) for partial funding via the 4DAir-MOLIS Project (contract No. 1150-852-71525). Fochesatto G.J. acknowledges support from NSF-grants 2117971, 2146929, and 2232282 from Physical Dynamic Meteorology, US-National Science Foundation.

Author Contributions D.A. and J.F. wrote and designed the main manuscript text. C.O. critically revised all the statistical components of the manuscript. R.J., J.F. and C.O. made substantial contributions in design and interpretation of data. All authors reviewed the manuscript.

Funding Open Access funding provided by Colombia Consortium

Data Availibility No datasets were generated or analysed during the current study.

Declarations

Conflict of interest The authors declare no competing interests.

References

Acevedo OC, Costa FD, Oliveira PES, Puhales FS, Degrazia GA, Roberti DR (2014) The influence of submeso processes on stable boundary layer similarity relationships. J Atmos Sci 71(1):207–225. https://doi.org/10.1175/JAS-D-13-0131.1

Angevine WM, Edwards JM, Lothon M, LeMone MA, Osborne SR (2020) Transition periods in the diurnally-varying atmospheric boundary layer over land. Boundary-Layer Meteorol 177(2–3):205–223. https://doi.org/10.1007/s10546-020-00515-y

Arya P, Holton J (2001) Introduction to micrometeorology. ISSN, Elsevier Science

Babić N, Večenaj V, De Wekker SFJ (2017) Spectral gap characteristics in a daytime valley boundary layer. Q J R Meteorol Soc 143(707):2509–2523. https://doi.org/10.1002/qj.3103

Chui CK (1992) An introduction to wavelets. No. v. 1 in wavelet analysis and its applications. Academic Press, Boston

Collineau S, Brunet Y (1993a) Detection of turbulent coherent motions in a forest canopy part I: wavelet analysis. Boundary-Layer Meteorol 65(4):357–379. https://doi.org/10.1007/BF00707033

Collineau S, Brunet Y (1993b) Detection of turbulent coherent motions in a forest canopy part II: time-scales and conditional averages. Boundary-Layer Meteorol 66(1–2):49–73. https://doi.org/10.1007/BF00705459

Donateo A, Cava D, Contini D (2017) A case study of the performance of different detrending methods in turbulent-flux estimation. Boundary-Layer Meteorol 164(1):19–37. https://doi.org/10.1007/s10546-017-0243-4

Eckley IA, Nason GP (2005) Efficient computation of the discrete autocorrelation wavelet inner product matrix. Stat Comput 15(2):83–92. https://doi.org/10.1007/s11222-005-6200-y

Farge M (1992) Wavelet transforms and their applications to turbulence. Annu Rev Fluid Mech 24(1):395–458. https://doi.org/10.1146/annurev.fl.24.010192.002143

Fochesatto GJ, Mayfield JA, Starkenburg D, Gruber MA, Conner J (2015) Occurrence of shallow cold flows in the winter atmospheric boundary layer of interior of Alaska. Meteorol Atmos Phys 127:369–382

Foken T, Kramm G (1995) On the determination of dry deposition and emission of gaseous compounds at the biosphere-atmosphere interface. Meteorologische Zeitschrift

Foken T, Wichura B (1996) Tools for quality assessment of surface-based flux measurements. Agric For Meteorol 78(1):83–105. https://doi.org/10.1016/0168-1923(95)02248-1

Foken T, Göockede M, Mauder M, Mahrt L, Amiro B, Munger W (2005) Post-field data quality control. In: Lee X, Massman W, Law B (eds) Handbook of micrometeorology, vol 29. Kluwer Academic Publishers, Dordrecht, pp 181–208. https://doi.org/10.1007/1-4020-2265-4_9

Guerrero O, Jimenez R (2014) Spatial representativeness of the bogota air quality monitoring network. In: Proceedings of the air and waste management Association's annual conference and exhibition, AWMA, vol 4, pp 2709–2716

Hojstrup J (1993) A statistical data screening procedure. Meas Sci Technol 4(2):153. https://doi.org/10.1088/0957-0233/4/2/003

Howell JF, Mahrt L (1997) Multiresolution flux decomposition. Boundary-Layer Meteorol 83(1):117–137. https://doi.org/10.1023/A:1000210427798

Kaimal JC, Finnigan JJ (1994) Atmospheric boundary layer flows: their structure and measurement. Oxford University Press, Oxford. https://doi.org/10.1016/0169-8095(95)00045-3

Kang SL (2009) Temporal oscillations in the convective boundary layer forced by mesoscale surface heat-flux variations. Boundary-Layer Meteorol 132(1):59–81. https://doi.org/10.1007/s10546-009-9391-5

Katul G, Chu C (1998) A theoretical and experimental investigation of energy-containing scales in the dynamic sublayer of boundary-layer flows. Boundary-Layer Meteorol 86:279–312. https://doi.org/10.1023/A:1000657014845

Katul G, Vidakovic B (1996) The partitioning of attached and detached eddy motion in the atmospheric surface layer using Lorentz wavelet filtering. Boundary-Layer Meteorol 77(2):153–172. https://doi.org/10.1007/BF00119576

Lehner M, Rotach MW (2023) The performance of a time-varying filter time under stable conditions over mountainous terrain. Boundary-Layer Meteorol 188(3):523–551. https://doi.org/10.1007/s10546-023-00824-y

Maillard J, Ravetta F, Raut JC, Fochesatto GJ, Law KS (2022) Modulation of boundary-layer stability and the surface energy budget by a local flow in Central Alaska. Boundary-Layer Meteorol 185(3):395–414. https://doi.org/10.1007/s10546-022-00737-2

Malingowski J, Atkinson D, Fochesatto J, Cherry J, Stevens E (2014) An observational study of radiation temperature inversions in Fairbanks, Alaska. Polar Sci 8(1):24–39. https://doi.org/10.1016/j.polar.2014.01.002

Mallat S (1989) A theory for multiresolution signal decomposition: the wavelet representation. IEEE Trans Pattern Anal Mach Intell 11(7):674–693. https://doi.org/10.1109/34.192463

Mayfield JA, Fochesatto GJ (2013) The layered structure of the winter atmospheric boundary layer in the interior of Alaska. J Appl Meteorol Climatol 52(4):953–973. https://doi.org/10.1175/JAMC-D-12-01.1

Morales LA (2020) Flujos de dióxido de carbono y vapor de agua medidos mediante covarianza de remolinos en sabana nativa y cultivos transitorios mecanizados en la altillanura colombiana. PhD thesis, Universidad Nacional de Colombia

Nappo C, Sun J, Mahrt L, Belušić D (2014) Determining wave-turbulence interactions in the stable boundary layer. Bull Am Meteorol Soc 95(1):ES11–ES13. https://doi.org/10.1175/BAMS-D-12-00235.1

Nason G (2008) Wavelet methods in statistics with R, 1st edn. Springer Publishing Company, Incorporated, Berlin

Nason GP, Von Sachs R, Kroisandt G (2000) Wavelet processes and adaptive estimation of the evolutionary wavelet spectrum. J R Stat Soc Ser B Stat Methodol 62(2):271–292. https://doi.org/10.1111/1467-9868.00231

Oncley SP, Friehe CA, Larue JC, Businger JA, Itsweire EC, Chang SS (1996) Surface-layer fluxes, profiles, and turbulence measurements over uniform terrain under near-neutral conditions. J Atmos Sci 53(7):1029–1044. https://doi.org/10.1175/1520-0469(1996)053<1029:SLFPAT>2.0.CO;2

Ortiz E, Jimenez R, Fochesatto GJ, Morales-Rincon LA (2019) Caracterización de la turbulencia atmosférica en una gran zona verde de una megaciudad tropical. Rev Acad Colomb Cienc 43(166):133–145

Park T, Eckley IA, Ombao HC (2014) Estimating time-evolving partial coherence between signals via multivariate locally stationary wavelet processes. IEEE Trans Signal Process 62(20)

Percival DP (1995) On estimation of the wavelet variance. Biometrika 82(3):619–631. https://doi.org/10.1093/biomet/82.3.619

Priestley MB (1982) Spectral analysis and time series

Sanderson J, Fryzlewicz P, Jones MW (2010) Estimating linear dependence between nonstationary time series using the locally stationary wavelet model. Biometrika 97(2):435–446. https://doi.org/10.1093/biomet/asq007

Shumway RH, Stoffer DS (2017) Time series analysis and its applications
Simpson WR, Mao J, Fochesatto GJ, Law KS, DeCarlo PF, Schmale J, Pratt KA, Arnold SR, Stutz J, Dibb JE, Creamean JM, Weber RJ, Williams BJ, Alexander B, Hu L, Yokelson RJ, Shiraiwa M, Decesari S, Anastasio C, D'Anna B, Gilliam RC, Nenes A, St Clair JM, Trost B, Flynn JH, Savarino J, Conner LD, Kettle N, Heeringa KM, Albertin S, Baccarini A, Barret B, Battaglia MA, Bekki S, Brado T, Brett N, Brus D, Campbell JR, Cesler-Maloney M, Cooperdock S, Cysneiros De Carvalho K, Delbarre H, DeMott PJ, Dennehy CJ, Dieudonné E, Dingilian KK, Donateo A, Doulgeris KM, Edwards KC, Fahey K, Fang T, Guo F, Heinlein LMD, Holen AL, Huff D, Ijaz A, Johnson S, Kapur S, Ketcherside DT, Levin E, Lill E, Moon AR, Onishi T, Pappaccogli G, Perkins R, Pohorsky R, Raut JC, Ravetta F, Roberts T, Robinson ES, Scoto F, Selimovic V, Sunday MO, Temime-Roussel B, Tian X, Wu J, Yang Y (2024) Overview of the Alaskan layered pollution and chemical analysis (ALPACA) field experiment. ACS ES&T Air 1(3):200–222. https://doi.org/10.1021/acsestair.3c00076
Starkenburg D, Fochesatto GJ, Prakash A, Cristóbal J, Gens R, Kane DL (2013) The role of coherent flow structures in the sensible heat fluxes of an Alaskan boreal forest. J Geophys Res Atmos 118(15):8140–8155. https://doi.org/10.1002/jgrd.50625
Starkenburg D, Metzger S, Fochesatto GJ, Alfieri JG, Gens R, Prakash A, Cristóbal J (2016) Assessment of despiking methods for turbulence data in micrometeorology. J Atmos Ocean Technol 33(9):2001–2013. https://doi.org/10.1175/JTECH-D-15-0154.1
Strunin MA, Hiyama T (2004) Applying wavelet transforms to analyse aircraft-measured turbulence and turbulent fluxes in the atmospheric boundary layer over eastern Siberia. Hydrol Process 18(16):3081–3098. https://doi.org/10.1002/hyp.5750
Stull RB (1988) An introduction to boundary layer meteorology. Springer Netherlands, Dordrecht
Taylor SAC, Park T, Eckley IA (2019) Multivariate locally stationary wavelet analysis with the mvLSW R package. J Stat Softw 90(11):1–19. https://doi.org/10.18637/jss.v090.i11
Taylor S, Park T, Eckley I, Killick R (2022) mvLSW: Multivariate, locally stationary wavelet process estimation
Torrence C, Compo GP (1998) A practical guide to wavelet analysis. Bull Am Meteorol Soc 79(1):61–78. https://doi.org/10.1175/1520-0477(1998)079<0061:APGTWA>2.0.CO;2
Vercauteren N, Boyko V, Kaiser A, Belušić D (2019) Statistical investigation of flow structures in different regimes of the stable boundary layer. Boundary-Layer Meteorol 173(2):143–164. https://doi.org/10.1007/s10546-019-00464-1
Vickers D, Mahrt L (1997) Quality control and flux sampling problems for tower and aircraft data. J Atmos Oceanic Technol 14(3):512–526. https://doi.org/10.1175/1520-0426(1997)014<0512:QCAFSP>2.0.CO;2
Vickers D, Mahrt L (2003) The cospectral gap and turbulent flux calculations. J Atmos Ocean Technol 20:13. https://doi.org/10.1175/1520-0426(2003)20<660:TCGATF>2.0.CO;2
Voronovich V, Kiely G (2007) On the gap in the spectra of surface-layer atmospheric turbulence. Boundary-Layer Meteorol 122(1):67–83. https://doi.org/10.1007/s10546-006-9108-y